Check for updates

Received: 5 September 2023 | Revised: 8 December 2023 | Accepted: 27 December 2023

DOI: 10.1002/mp.16943

RESEARCH ARTICLE

MEDICAL PHYSICS

Reduction of cone-beam CT artifacts in a robotic CBCT device using saddle trajectories with integrated infrared tracking

Chengtao Wei[1,2] | **Johanna Albrecht**[1,2] | **Simon Rit**[3] | **Matthieu Laurendeau**[3,4] | **Adrian Thummerer**[1] | **Stefanie Corradini**[1] | **Claus Belka**[1,5,6] | **Philipp Steininger**[7] | **Felix Ginzinger**[7] | **Christopher Kurz**[1] | **Marco Riboldi**[2] | **Guillaume Landry**[1]

[1]Department of Radiation Oncology, LMU University Hospital, LMU Munich, Munich, Germany

[2]Department of Medical Physics, Ludwig-Maximilians-Universität München, Garching, Germany

[3]Univ Lyon, INSA-Lyon, Université Claude Bernard Lyon 1, UJM-Saint Etienne, CNRS, Inserm, CREATIS UMR 5220, U1294, F-69373, Lyon, France

[4]Thales AVS, Moirans, France

[5]German Cancer Consortium (DKTK), Partner Site Munich, Munich, Germany

[6]German Cancer Consortium (DKTK), partner site Munich, a partnership between DKFZ and LMU University Hospital Munich, Munich, Germany

[7]Research & Development, medPhoton GmbH, Salzburg, Austria

Correspondence
Guillaume Landry, Department of Radiation Oncology, LMU University Hospital, LMU Munich, Munich, Germany.
Email: guillaume.landry@med.uni-muenchen.de

Funding information
Deutsche Forschungsgemeinschaft, Grant/Award Number: INST 86/2120-1 FUGG

Abstract

Background: Cone beam computed tomography (CBCT) is widely used in many medical fields. However, conventional CBCT circular scans suffer from cone beam (CB) artifacts that limit the quality and reliability of the reconstructed images due to incomplete data.

Purpose: Saddle trajectories in theory might be able to improve the CBCT image quality by providing a larger region with complete data. Therefore, we investigated the feasibility and performance of saddle trajectory CBCT scans and compared them to circular trajectory scans.

Methods: We performed circular and saddle trajectory scans using a novel robotic CBCT scanner (Mobile ImagingRing (IRm); medPhoton, Salzburg, Austria). For the saddle trajectory, the gantry executed yaw motion up to $\pm 10°$ using motorized wheels driving on the floor. An infrared (IR) tracking device with reflective markers was used for online geometric calibration correction (mainly floor unevenness). All images were reconstructed using penalized least-squares minimization with the conjugate gradient algorithm from RTK with $0.5 \times 0.5 \times 0.5$ mm^3 voxel size. A disk phantom and an Alderson phantom were scanned to assess the image quality. Results were correlated with the local incompleteness value represented by $\tan(\psi)$, which was calculated at each voxel as a function of the source trajectory and the voxel's 3D coordinates. We assessed the magnitude of CB artifacts using the full width half maximum (FWHM) of each disk profile in the axial center of the reconstructed images. Spatial resolution was also quantified by the modulation transfer function at 10% (MTF10).

Results: When using the saddle trajectory, the region without CB artifacts was increased from 43 to 190 mm in the SI direction compared to the circular trajectory. This region coincided with low values for $\tan(\psi)$. When $\tan(\psi)$ was larger than 0.02, we found there was a linear relationship between the FWHM and $\tan(\psi)$. For the saddle, IR tracking allowed the increase of MTF10 from 0.37 to 0.98 lp/mm.

Conclusions: We achieved saddle trajectory CBCT scans with a novel CBCT system combined with IR tracking. The results show that the saddle

Marco Riboldi and Guillaume Landry contributed equally to this study.

This is an open access article under the terms of the Creative Commons Attribution License, which permits use, distribution and reproduction in any medium, provided the original work is properly cited.

© 2024 The Authors. *Medical Physics* published by Wiley Periodicals LLC on behalf of American Association of Physicists in Medicine.

trajectory provides a larger region with reliable reconstruction compared to the circular trajectory. The proposed method can be used to evaluate other non-circular trajectories.

KEYWORDS
CBCT, cone beam artifact, data insufficiency, infrared tracking, robotic, saddle trajectories

1 | INTRODUCTION

Cone beam computed tomography (CBCT) is playing an important role in many medical fields, such as dentistry,[1,2] image-guided radiotherapy,[3–5] image-guided surgery,[6,7] and brachytherapy[8] due to its low cost and flexibility. However, CBCT is still largely limited by its poor image quality with low contrast to noise ratio, and various artifacts. Among these, cone beam (CB) artifacts come from insufficient projection sampling. CB artifacts can lead to streaks, shading, and distortion of edges. The severity of CB artifacts will increase as a point gets further from the central axial plane containing the circular source trajectory. Tuy's condition states that each point P of the object can be reconstructed if every plane passing through P intersects at least once with the trajectory.[9] Finch showed that this condition is necessary.[10] Therefore, for a conventional circular trajectory CBCT scan, only the central plane can be reliably reconstructed.

Recently, many studies using unconventional trajectories to improve CBCT image quality were reported. Tilted circular trajectories were used to improve the image quality near the skull base,[11] reduce the dose to eye lenses[12] and improve localization in CT-guided biopsies.[13] Tersol et al. investigated reducing CB artifacts using tilted circular trajectories.[14] Task-based noncircular trajectories were also explored to eliminate the influence of CB artifacts,[15–17] with parameterized trajectories based on information on patient and metal implants to reduce metal and CB artifacts. Many other non-circular trajectories were also proposed, for example, sinusoidal trajectory,[18–20] helical trajectory,[21–23] circle-and-line trajectory[24] and circle-and-arc trajectory.[25]

A practical type of non-circular trajectory is the saddle trajectory. It has been proven that exact reconstruction is possible for a saddle trajectory scan even if there is axial truncation.[26] Geometrically, Tuy's condition is satisfied inside the convex hull of the saddle trajectory, which means that it should provide a much larger reliable reconstruction region than the circular trajectory.

Even if the source trajectory was perfectly known, artifacts might arise due to incomplete projection data. To quantitatively assess the extent to which a voxel violates Tuy's condition, we used the incompleteness metric suggested by Clackdoyle et al.[27] Instead of using a binary criterion to judge whether a voxel satisfies the Tuy condition, the incompleteness metric provides a continuous value to assess the performance of the trajectory. The incompleteness value is a geometric quantity representing the data sufficiency according to Tuy's condition of one voxel P in a given direction. A smaller incompleteness value means Tuy's condition is less violated for P. Sun et al. showed there were no obvious CB artifacts when the local incompleteness value is smaller than 0.02.[28] Moreover, the incompleteness metric is independent of the reconstruction algorithm, therefore can be used as a general method to assess the performance of arbitrary trajectories.[14,28]

A practical problem related to non-circular trajectory scans is that we must specify the exact positions and directions of the source and detector in a fixed coordinate system for every projection to achieve high spatial resolution reconstruction. Although we can roughly infer the position from the CBCT system geometry, errors can come from many aspects including calibration uncertainties and reproducibility in the execution of the trajectory, for example from driving over an uneven floor in our case. Therefore, online calibration adjustments are needed for an irregular trajectory scan.

In this paper, we investigated the feasibility of saddle trajectory CBCT scans which used infrared (IR) tracking for online geometric calibration for the first time. It is also the first evaluation of a clinical system that has built-in saddle trajectory programs. Images were reconstructed using iterative and analytical reconstruction combined with IR tracking geometric corrections. We quantitatively assessed the CB artifacts and related them to the incompleteness metric.

2 | METHODS AND MATERIALS

2.1 | Mobile CBCT scanner

The robotic mobile CBCT scanner used in this work (Mobile ImagingRing (IRm); medPhoton, Salzburg, Austria) was a novel mobile CBCT scanner that can perform robotic movements during a scan, including tilt and yaw of the gantry as well as combined linear translations on the floor (see Figure 1a). The motorized wheels underneath enabled the whole CBCT scanner to move in four directions and rotate around a certain vertical axis to perform a yaw saddle trajectory. Figure 1b shows the system, while a sketch of the geometrical parameters is

24734209, 0, Downloaded from https://aapm.onlinelibrary.wiley.com/doi/10.1002/mp.16943 by Cochrane Germany, Wiley Online Library on [21/02/2024]. See the Terms and Conditions (https://onlinelibrary.wiley.com/terms-and-conditions) on Wiley Online Library for rules of use; OA articles are governed by the applicable Creative Commons License

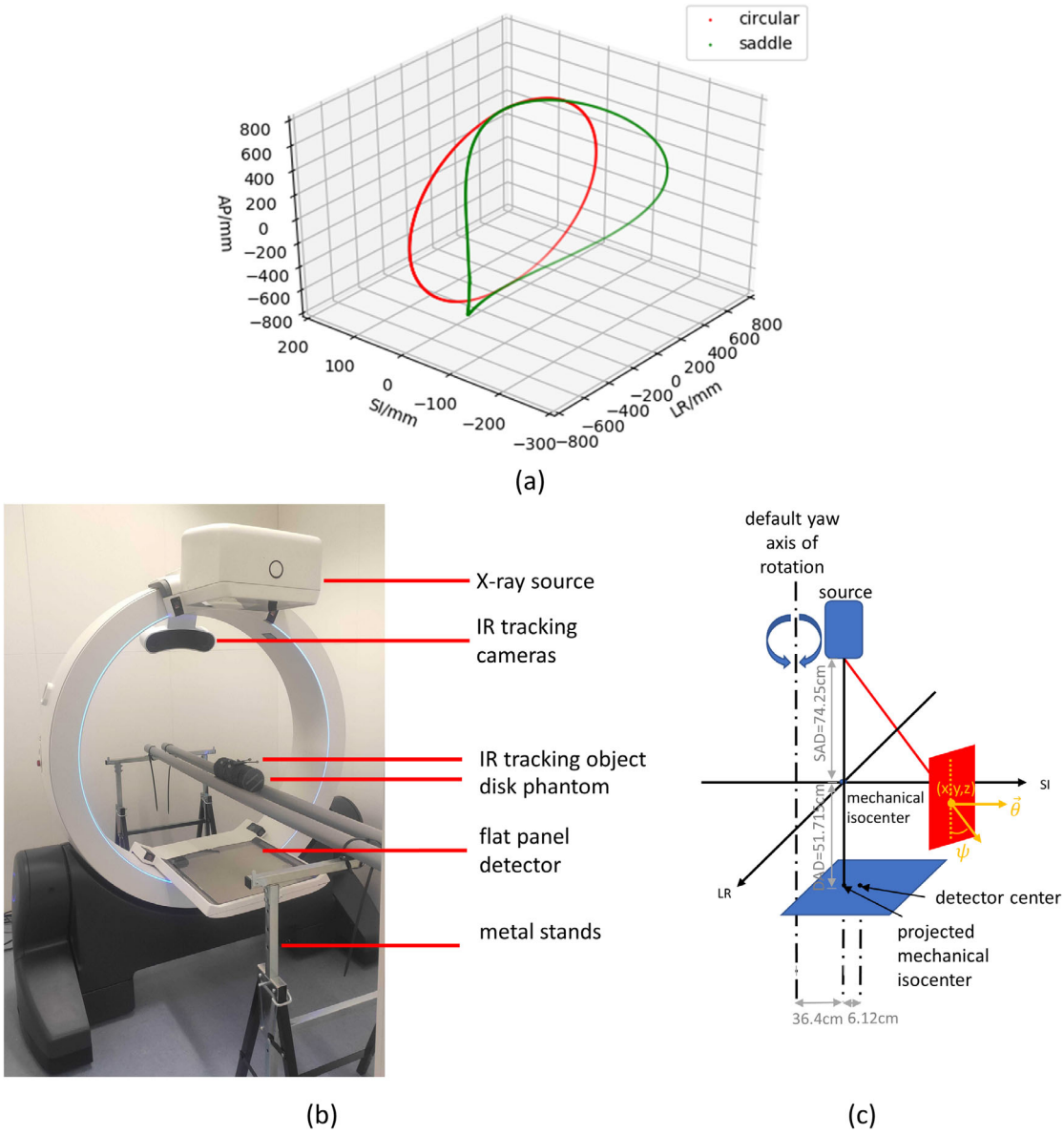

FIGURE 1 Scan setup and geometry illustration. (a) Yaw-based saddle trajectory and circular trajectory. (b) Disk phantom upon two polyvinyl chloride pipes along SI direction. Also visible are the tracking cameras mounted on top of the gantry, and the tracking object with markers on the phantom. (c) The geometry of the used CBCT system is shown in blue. Illustrations of $\tan(\psi)$ are in red and orange. SAD stands for source axis distance and DAD for detector axis distance. CBCT, Cone Beam Computed Tomography; SI, superior-inferior.

shown in Figure 1c. The scan parameters are given in Table 1.

2.2 | Geometry and IR tracking

The scanning geometry information could be obtained from the projection files of every scan, which included the yaw angle in fixed coordinates and positions and directions of the detector in the ring gantry coordinate system (independent of the yaw angle). With this, the scan trajectory could be obtained by applying the transformation to source and detector positions and directions according to the geometric information reported by the motor encoders (yaw angle and location of yaw rotation axis as reported by the manufacturer). This was called nominal geometry. For circular scans, the vendor's geometric calibration based on Keuschnigg et al., Zechner et al.,[29,30] and focal spot position calibration based on Messner et al.[31] were applied, and the same was also applied to yaw scans. However, for yaw scans these data might not be accurate due to practical limitations, such as an uneven floor and vibrations. Therefore, a motion capture device was used in this study to correct geometrical errors.

24734209, 0, Downloaded from https://aapm.onlinelibrary.wiley.com/doi/10.1002/mp.16943 by Cochrane Germany, Wiley Online Library on [21/02/2024]. See the Terms and Conditions (https://onlinelibrary.wiley.com/terms-and-conditions) on Wiley Online Library for rules of use; OA articles are governed by the applicable Creative Commons License

TABLE 1 Settings used for circular and the saddle trajectory on the scanner.

Acquisition		
	Circular trajectory	**Saddle trajectory**
Sequence name	**full-scan (360 deg circular)**	**full-scan (360 deg saddle)**
Acquisition time	60 s	
Radiation	Constant pulsed[a]	
Energy	120 kV	
Exposure per projection	20 ms, 5 mA	
Active detector settings	1440×1440 px^2, 12 fps (166 ms), gain 5 (114 e/ADU)	
Filtration	0.5 mm Cu	
Collimation jaws	Fully open	
Source to axis distance	742.5 mm	
Source to detector distance	1259.65 mm	
Detector size	432×432 mm^2	
Projection number	720	
Reconstruction: iterative		
Voxel size	$0.5 \times 0.5 \times 0.5$ mm^3	
Iteration number	50	
Reconstruction method	Conjugate gradient	
Regularization weight (γ)	10	
Reconstruction time	18 min 8 s	18 min 15 s
Reconstruction: FDK		
Voxel size	$0.5 \times 0.5 \times 0.5$ mm^3	
Filter	Hann Filter w/ (Hann=HannY=1), w/o (Hann=HannY=0)	
Reconstruction time	32 s	32 s
Hardware		
GPU	Nvidia RTX A6000	
CPU	Intel Xeon Gold 6354	
CPU RAM	384 Gb	

aRadiation in pulsed mode with a constant pulse length and frequency.

We used two IR cameras and a tracking object (Rigid Body Marker Base, MCP1145; NaturalPoint, Inc., Corvallis, USA) to acquire the motion data. These IR cameras were provided by the vendor as optional assemblies mounted to their scanner's gantry and attached to the scanner gantry, thus moving together with it and independent from the source and detector during yaw motion. The motion data was acquired by tracking the position and direction of a rigid object with six reflective markers which was statically positioned during the scan. During every scan, the object was put on top of the phantom so that both cameras could see all the markers. For every projection, the position and direction of the marker object were recorded and saved as a translation vector $t = (x, y, z)$ and the corresponding pose as a quaternion object in the geometry files. A quaternion object was defined with four real numbers (q_0, q_1, q_2, q_3) and three imaginary orthogonal unit vectors $\vec{i}, \vec{j}, \vec{k}$. To get the transformation matrix from the quaternion, the following matrix was used for calculation:

$$R = \begin{bmatrix} 1 - 2{q_2}^2 - 2{q_3}^2 & 2q_1q_2 - 2q_0q_3 & 2q_1q_3 + 2q_0q_2 \\ 2q_1q_2 + 2q_0q_3 & 1 - 2{q_1}^2 - 2{q_3}^2 & 2q_2q_3 - 2q_0q_1 \\ 2q_1q_3 - 2q_0q_2 & 2q_2q_3 + 2q_0q_1 & 1 - 2{q_1}^2 - 2{q_2}^2 \end{bmatrix}. \tag{1}$$

For the geometrical corrections, the source positions s, detector positions d, and the vectors u and v which spanned the edges of the detector were first acquired from the geometry file. Then these values were corrected by the following equations:

$$\begin{aligned} s' &= R_0 R^{-1}(s - t) + t_0, \\ d' &= R_0 R^{-1}(d - t) + t_0, \\ u' &= R_0 R^{-1} u, \\ v' &= R_0 R^{-1} v, \end{aligned} \tag{2}$$

24734209, 0, Downloaded from https://aapm.onlinelibrary.wiley.com/doi/10.1002/mp.16943 by Cochrane Germany, Wiley Online Library on [21/02/2024]. See the Terms and Conditions (https://onlinelibrary.wiley.com/terms-and-conditions) on Wiley Online Library for rules of use; OA articles are governed by the applicable Creative Commons License

where R_0 and t_0 were the quaternion transformation matrix and tracking object position calculated from the first frame. R and t were the quaternion transformation matrix and tracking object position from the current frame. This yielded the corrected source and detector positions and directions (s', d', u', v'). All the source and detector positions were calculated with respect to the first frame. This was labeled the measured geometry. The geometry calibration could be done both online and offline.

2.3 | Reconstruction algorithm

We used the penalized least-squares minimization with the conjugate gradient algorithm and the FDK algorithm from the Reconstruction Toolkit (RTK) software package (version 2.3.0)[32] to reconstruct all the images. RTK's implementation of FDK accounts for the source and detector positions and is therefore applicable to saddle trajectories for approximate filtered backprojection reconstruction. The regularization term for the iterative reconstruction was the squared norm of the gradient. The number of iterations is shown in Table 1. For the FDK reconstruction, we reconstructed the image both with a Hann filter and without a Hann window on the ramp filter. The voxel size of the reconstructed image was $0.5 \times 0.5 \times 0.5$ mm^3. In general, reconstructions were performed using either the encoder-reported positions from the projection files' nominal geometry metadata (nominal geometry), or with the positions obtained from the IR tracking device (measured geometry). When using the measured geometry, it was necessary to apply a rigid transformation to account for the arbitrary position and orientation of the first frame (which was acquired with a yaw angle of 10°). This registration was determined empirically by registering initial reconstructions using the nominal and measured geometries.

2.4 | Phantoms to assess CB artifact

Two phantoms were used in our study. The first phantom was a disk phantom made of a series of 1 mm thick and 100 mm diameter acrylic disks separated by 20 mm foam spacers. This phantom enabled us to see obvious CB artifacts along the normal to the disks. The second phantom we used was the head section of the Alderson Phantom, which allowed visualization of the CB artifact at the interface of the slabs composing the phantom.

2.5 | Simulation of saddle trajectories

In addition to the experimental scans defined below, circular and saddle trajectory simulations were done. A voxelized digital disk phantom was generated with the same parameters as the real phantom. The scanning geometry was also obtained from experimental geometry files, including their IR tracking information, source and detector position. The voxelized phantom had an image size of $360 \times 360 \times 371$ voxels and a voxel size of $1 \times 1 \times 1$ mm^3. The phantom was first forward-projected to digitally reconstructed radiographs using the nominal scan geometry, then reconstructed following the same workflow and parameters as shown in Table 1. We virtually positioned the phantom at several positions in the scan region to scan the relation between the artifact and the incompleteness metric. We did not align it exactly with the experimental phantom since we were interested in the general trends of the CB artifact.

2.6 | Acquisition

The disk phantom was put upon two polyvinyl chloride pipes, which were supported by two metal stands that were outside the x-ray beam. This setup ensured that the phantom stayed static during the scan. To show the CB artifacts, the disk phantom symmetry axis was put along the superior-inferior (SI) direction. The tracking object was placed on the phantom and was visible by the two tracking cameras throughout the scan.

For the circular and saddle trajectory scans, the image center and the phantom center were aligned manually using the IRm laser crossing. Then the field of view (FOV) was set manually to contain the whole phantom and keep the collimator jaws fully open. During the scan, the yaw angle D was a function of amplitude $A = 10°$, source rotation angle x, and phase $\phi = 180°$. As shown in Figure 1a, the maximum offset for the source was when the source with respect to the circular scan was positioned laterally ($x = 90°$, which was the starting position for the scan).

$$D = A \cdot \sin(x + \phi) \tag{3}$$

2.7 | Quantification of results

2.7.1 | Data incompleteness

According to Tuy's sufficiency condition for untruncated projections, if for every plane intersecting the object there exists at least one source position in the plane, then accurate reconstruction is possible. This condition provides a binary criterion to assess whether the image can be exactly reconstructed or not. In practice, not all images failing this condition show obvious artifacts and the severity of the artifacts is not always the

24734209, 0, Downloaded from https://aapm.onlinelibrary.wiley.com/doi/10.1002/mp.16943 by Cochrane Germany, Wiley Online Library on [21/02/2024]. See the Terms and Conditions (https://onlinelibrary.wiley.com/terms-and-conditions) on Wiley Online Library for rules of use; OA articles are governed by the applicable Creative Commons License

same. Therefore, the incompleteness metric suggested by Clackdoyle et al. was used to quantify the extent to which a voxel deviated from Tuy's condition.[27]

The incompleteness of a voxel at point P was calculated by the following procedures: First, the source position was acquired and transformed according to the motion information acquired by the IR tracking cameras. Then for all the projection lines passing through the voxel, we calculated and kept those projection lines that fell on the detector, following the approach of Sun et al.[28] Third, for one specific direction θ, we took the lowest $\tan(\psi)$ from all the source positions. Finally, we took the largest $\tan(\psi)$ value from all directions as the incompleteness value for this voxel. Here ψ was the angle between the plane and the projection line. The red and orange parts of Figure 1c show the geometry of this calculation. For the calculation, we assumed that the whole object was within the FOV and that there was no truncation. We only calculated the incompleteness for the center of every voxel. Due to the discretization of the source trajectory, we actually calculated 720 projection lines for one voxel and took 576 points uniformly distributed on the unit hemisphere to represent the unit vectors θ.

2.7.2 | Convex hull

For the saddle trajectory, a convex hull is defined as the union of all chords. In our study, the convex hull was generated as a binary map depending on whether the point was inside the convex hull or not. Our convex hull was computed by connections of all source points. The binary map had dimensions $600 \times 600 \times 600$ voxels, and size $1600 \times 1600 \times 1600$ mm^3. This map had the same origin and scale as the reconstructed image, therefore could be overlayed to evaluate the image quality inside the convex hull.

2.7.3 | Artifact quantification using FWHM

To find the relationship between the $\tan(\psi)$ metric and artifacts, we used the reconstructed disk thickness at the disk center as a measure of the severity of artifacts. Due to the CB artifacts, the disks were distorted to a spindle shape. At the center of the disk, the artifacts were most pronounced. Therefore, we plotted the center profile of the phantom and measured the full width at half maximum (FWHM) for every disk. This metric was only to represent the artifact severity at the disk center, which meant we only used the FWHM of the disk to compare with the incompleteness value in the center point of the disk. This was done for both experimental acquisitions and simulations.

2.7.4 | Quantification of calibration correction

Since the IR tracking corrections were done according to the first frame of the scan, an arbitrary transformation, corresponding to the position of the first frame, was introduced in the measured geometry. For the yaw trajectory, this corresponded to a rotation of approximately 10° around the yaw axis. To be able to evaluate the magnitude of the IR correction, we used a registration algorithm to first register the measured geometry to the nominal geometry. Then we computed the difference between the nominal and measured geometries for the components of s, d, u, and v. For each pair of points, we calculated the difference by:

$$\begin{aligned} \Delta s &= Ts' - s, \\ \Delta d &= Td' - d, \\ \Delta u &= Tu' - u, \\ \Delta v &= Tv' - v, \end{aligned} \tag{4}$$

where T is the rigid registration matrix. The direction vector differences were expressed as three Euler angle components $(\Delta u_\phi, \Delta u_\psi, \Delta u_\theta)$ and $(\Delta v_\phi, \Delta v_\psi, \Delta v_\theta)$, which were calculated in the 321 (ZYX) sequence. We did this for 10 consecutive scans and calculated the mean correction and the standard deviation.

2.7.5 | Modulation transfer function

To quantify the spatial resolution in the axial plane with and without IR tracking, we scanned a cylinder phantom along the SI direction and calculated the modulation transfer function (MTF) from the radial edge-spread function (ESF) for each slice in the SI direction.[33] The cylinder phantom was 152 mm in diameter and was scanned with a detector pixel size of 0.3 mm. For comparison, we also used a previous scan of a cylinder phantom with 140 mm diameter using Elekta's XVI CBCT system with a detector pixel size of 0.8 mm. All the images were reconstructed with $0.5 \times 0.5 \times 0.5$ mm^3 voxel size. As the MTF might vary along the SI direction, we calculated the MTF for every slice and took the mean value. We calculated the MTF for the FDK reconstruction to avoid issues with iterative reconstruction such as noise and contrast dependence.[34] We did this with and without the Hann filter to determine the maximum resolution as well as a more practical resolution with reduced noise.

24734209, 0, Downloaded from https://aapm.onlinelibrary.wiley.com/doi/10.1002/mp.16943 by Cochrane Germany, Wiley Online Library on [21/02/2024]. See the Terms and Conditions (https://onlinelibrary.wiley.com/terms-and-conditions) on Wiley Online Library for rules of use; OA articles are governed by the applicable Creative Commons License

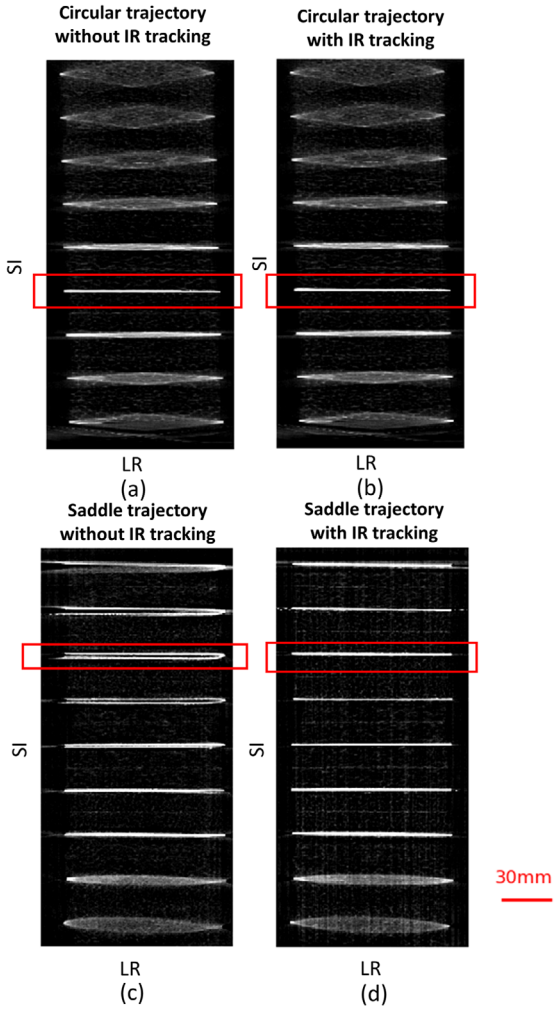

FIGURE 2 Disk phantom with and without IR tracking correction for the (a,b) circular and the (c,d) saddle scans. The red box indicates the major difference between (b,d) using IR tracking correction and (a,c) not using IR tracking correction. (window level: 0.0051, window width: 0.0097). IR, infrared.

3 | RESULTS

3.1 | IR tracking

Four coronal planes of the reconstructed images of the disk phantom with and without IR tracking are shown in Figure 2. For circular trajectory scans, no obvious difference could be found when using IR tracking or not (Figure 2a and 2b). In the saddle trajectory scans (Figure 2c), reconstructed disks on the upper part of the image show clear double structures when IR tracking was not used. No double structures were observed in Figure 2d when using IR tracking to correct the nominal geometry. IR tracking correction was used when reconstructing the rest of the scans shown in this paper. Figure S1 and Figure S2 additionally show the impact of IR tracking for the Alderson phantom where similar improvements were observed. The calibration corrections for the source and detector are shown in Figure 3. The position correction amplitudes for the source and detector are about 2 mm at most and the direction correction amplitudes are around 0.15°. From the figure, we can also see that the variation between the 10 scans can be relatively large, for example, the detector direction correction Δu_ϕ varies from 0.1° to −0.2°.

3.2 | Disk phantom

Four coronal and sagittal reconstruction planes are shown in Figure 4. The solid lines are isolines of $\tan(\psi)$ representing data incompleteness. Due to the CB artifacts, some reconstructed disks were distorted into spindle shapes. Both the circular trajectory and saddle trajectory scans showed that a larger incompleteness value corresponded to a more severe CB artifact. The reconstructed disks in the low incompleteness region ($\tan(\psi) < 0.02$) were all artifact-free.

Figure 4 also shows that the saddle trajectory scan had a much larger region with low incompleteness than the circular trajectory scan. For the circular trajectory, the shape of the low incompleteness region was approximately a cylinder in SI direction with a length of 43 mm and a diameter of 255 mm. For the saddle trajectory scan, the low incompleteness region was an irregular cylinder of 190 mm in SI, and its cross-section normal to SI had a short axis of 255 mm and a long axis of 270 mm. We could observe that the convex hull covered a smaller region in SI than the area where $\tan(\psi) < 0.02$.

3.3 | Relation between FWHM and incompleteness

Figure 5 reveals a strong relationship between the incompleteness $\tan(\psi)$ and the severity of the CB artifacts. For the circular trajectory, both the simulation and the experiment showed a linear relationship between incompleteness and FWHM. Most of the reconstructed disks had an FWHM larger than 1 mm, indicating that most reconstructed disks in the image show artifacts. As shown in Figure 4a, for the circular trajectory, only the disk on the trajectory plane was artifact-free.

For the saddle trajectory scan, most points were located at the low $\tan(\psi)$ region, as shown in the zoomed panel of Figure 5b. These points all had FWHMs around 1 mm, which was the thickness of the disks. For the disks outside of this region, their FWHM also showed a linear relationship with $\tan(\psi)$ similar to the circular trajectory.

3.4 | Alderson phantom

Figure 6 shows the coronal and axial view of the Alderson phantom scan. We could use the gaps between

24734209, 0, Downloaded from https://aapm.onlinelibrary.wiley.com/doi/10.1002/mp.16943 by Cochrane Germany, Wiley Online Library on [21/02/2024]. See the Terms and Conditions (https://onlinelibrary.wiley.com/terms-and-conditions) on Wiley Online Library for rules of use; OA articles are governed by the applicable Creative Commons License

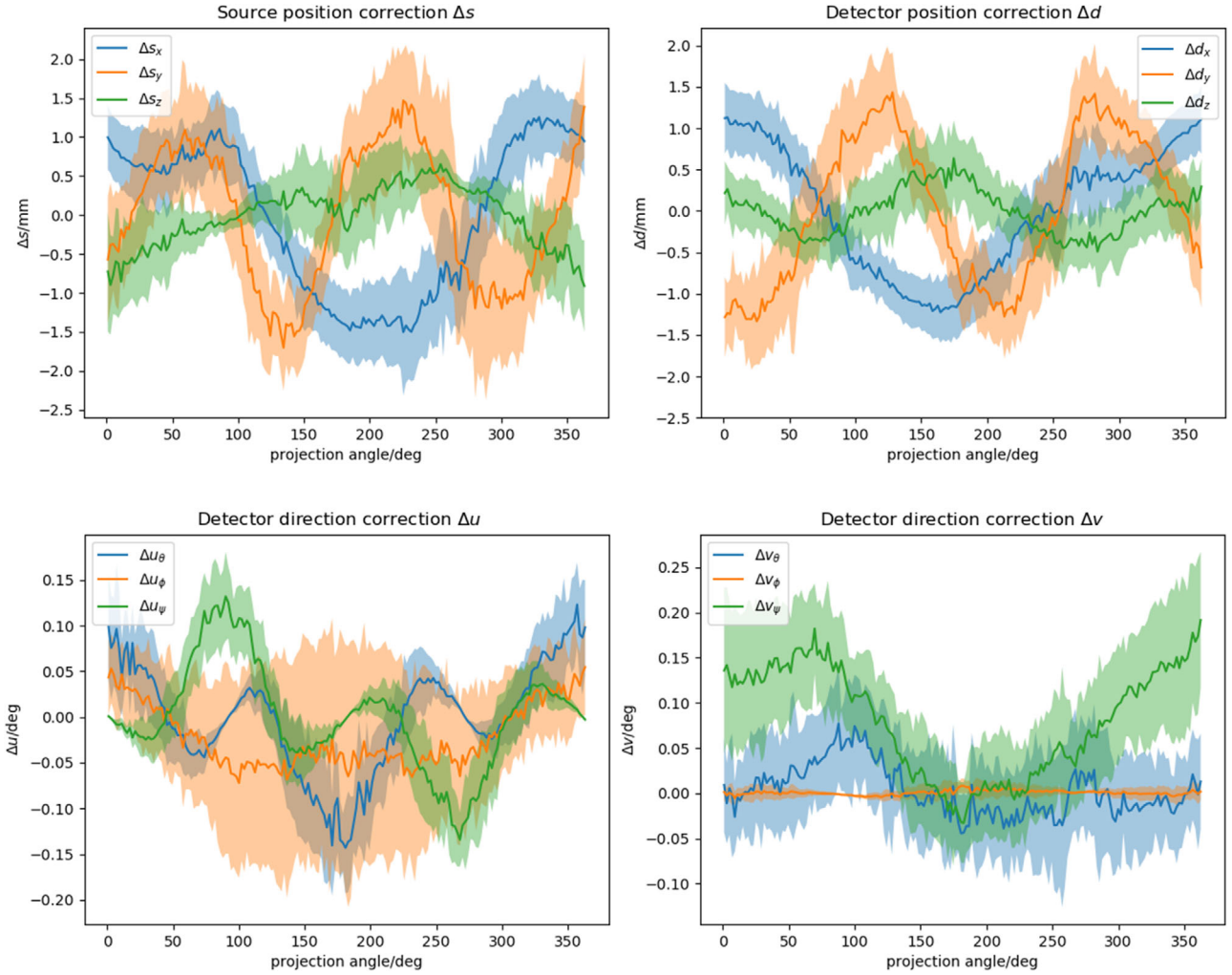

FIGURE 3 (top) Three translational corrections for source and detector positions using IR tracking. (bottom) Detector direction corrections using IR tracking in Euler angles. The corrections were obtained from 10 different yaw-based saddle trajectory scans. The solid lines are the average and the shaded area represents one standard deviation.

slabs to assess the magnitude of the CB artifact. We saw that for the circular trajectory, areas outside the $\tan(\psi) < 0.02$ region showed distortion of the gaps, which were almost invisible. For the saddle trajectory, the $\tan(\psi) < 0.02$ region was larger and the gaps in that region were well reconstructed. Outside of the region, the gaps were also distorted in the saddle scan. Similar effects were observed at the flat part at the top of the phantom head. Figure S3 also shows the coronal and axial images reconstructed using FDK reconstruction with Hann filtering.

3.5 | Spatial resolution

Table 2 reports the MTF10 values for the circular and saddle scans with and without IR tracking. The spatial resolutions are almost the same for circular trajectories with and without IR tracking. For the saddle trajectory, IR tracking correction greatly improved the spatial resolution from 0.37 to 0.98 lp/mm, which was at the same level as XVI CBCT. When applying the Hann filter (corresponding to the reconstruction settings of Figure S3), the spatial resolution of the circular and saddle trajectories decreased by 84% and 91%, respectively. The XVI resolution was further reduced due to the larger detector pixel size's impact on the adaptive Hann filter's maximum frequency.

4 | DISCUSSION

In this work, we investigated the feasibility and performance of a saddle CBCT scan trajectory. With the help of the incompleteness value, we found that when the incompleteness value was smaller than 0.02, there were no obvious artifacts in the reconstructed images. The same threshold was also reported by Sun et al.[28]

24734209, 0, Downloaded from https://aapm.onlinelibrary.wiley.com/doi/10.1002/mp.16943 by Cochrane Germany, Wiley Online Library on [21/02/2024]. See the Terms and Conditions (https://onlinelibrary.wiley.com/terms-and-conditions) on Wiley Online Library for rules of use; OA articles are governed by the applicable Creative Commons License

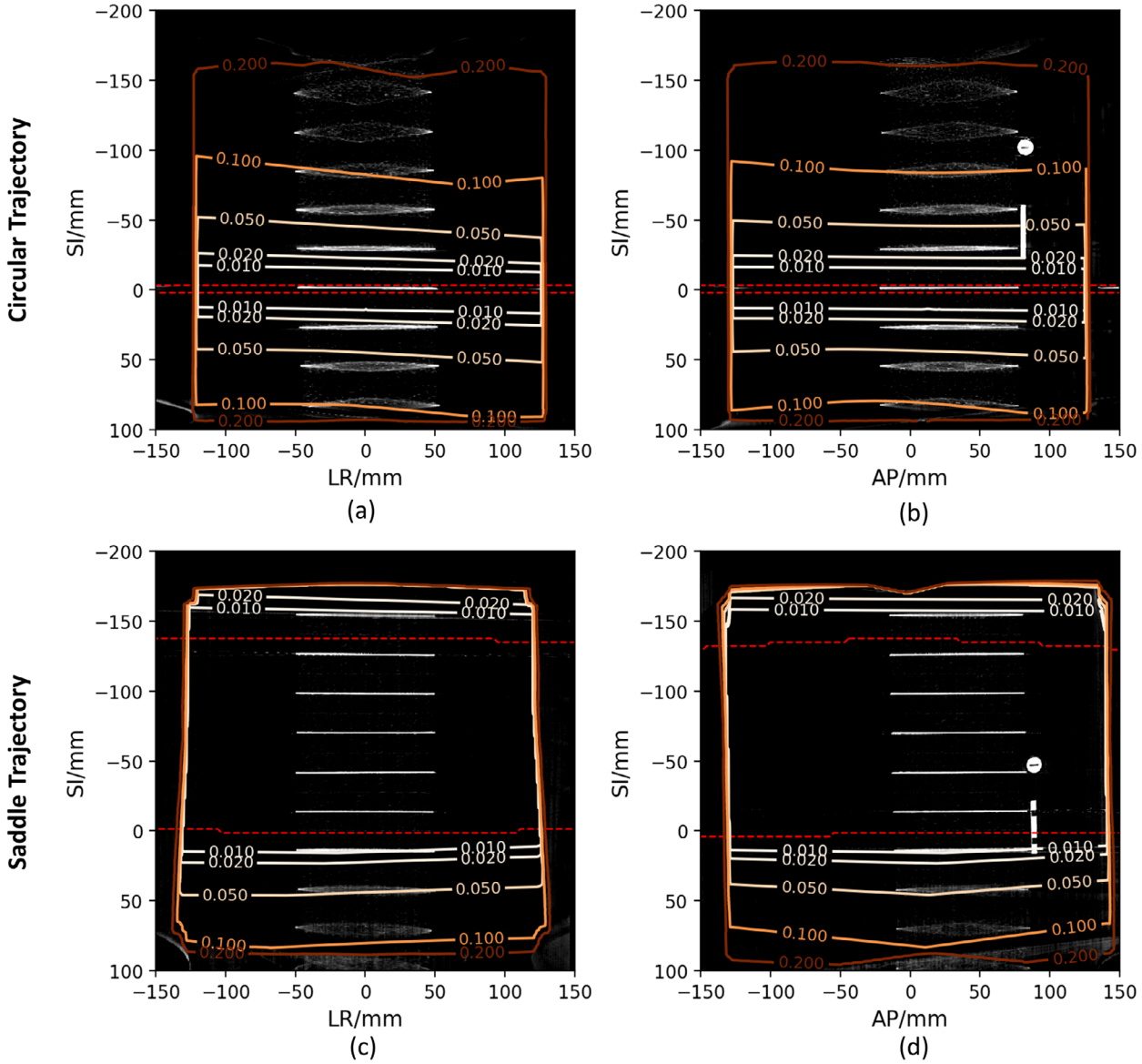

FIGURE 4 Disk phantom with tan(ψ) plot. (a,b) Coronal and sagittal planes of circular trajectory scan. (c,d) Coronal and sagittal planes of saddle trajectory scan. Solid lines are isolines of tan(ψ). Red dashed lines are the edges of the convex hull region. (window level: 0.0082, window width: 0.0136).

TABLE 2 MTF10 for different trajectories and settings.

	circle with IR tracking lp/mm	circle w/o IR tracking	saddle with IR tracking	saddle w/o IR tracking	XVI CBCT
FDK w/o Hann	1.39 ± 0.06	1.39 ± 0.04	0.98 ± 0.07	0.37 ± 0.04	1.00 ± 0.012
FDK with Hann[a]	1.18 ± 0.02	1.18 ± 0.02	0.9 ± 0.05	0.30 ± 0.02	0.66 ± 0.003

aHann filter will have a larger effect on XVI due to the larger detector pixel size of 0.8 mm.

In comparison with the conventional circular trajectory, the saddle trajectory provided a much larger region with low incompleteness. In correspondence, CB artifacts in the saddle trajectory scan images were largely reduced.

Figure 2 demonstrates that for saddle trajectory scans, new artifacts might be introduced in the image without IR tracking corrections. These artifacts might come from practical limitations such as vibrations and uneven floors. During the circular scan, the gantry stayed

24734209, 0, Downloaded from https://aapm.onlinelibrary.wiley.com/doi/10.1002/mp.16943 by Cochrane Germany, Wiley Online Library on [21/02/2024]. See the Terms and Conditions (https://onlinelibrary.wiley.com/terms-and-conditions) on Wiley Online Library for rules of use; OA articles are governed by the applicable Creative Commons License

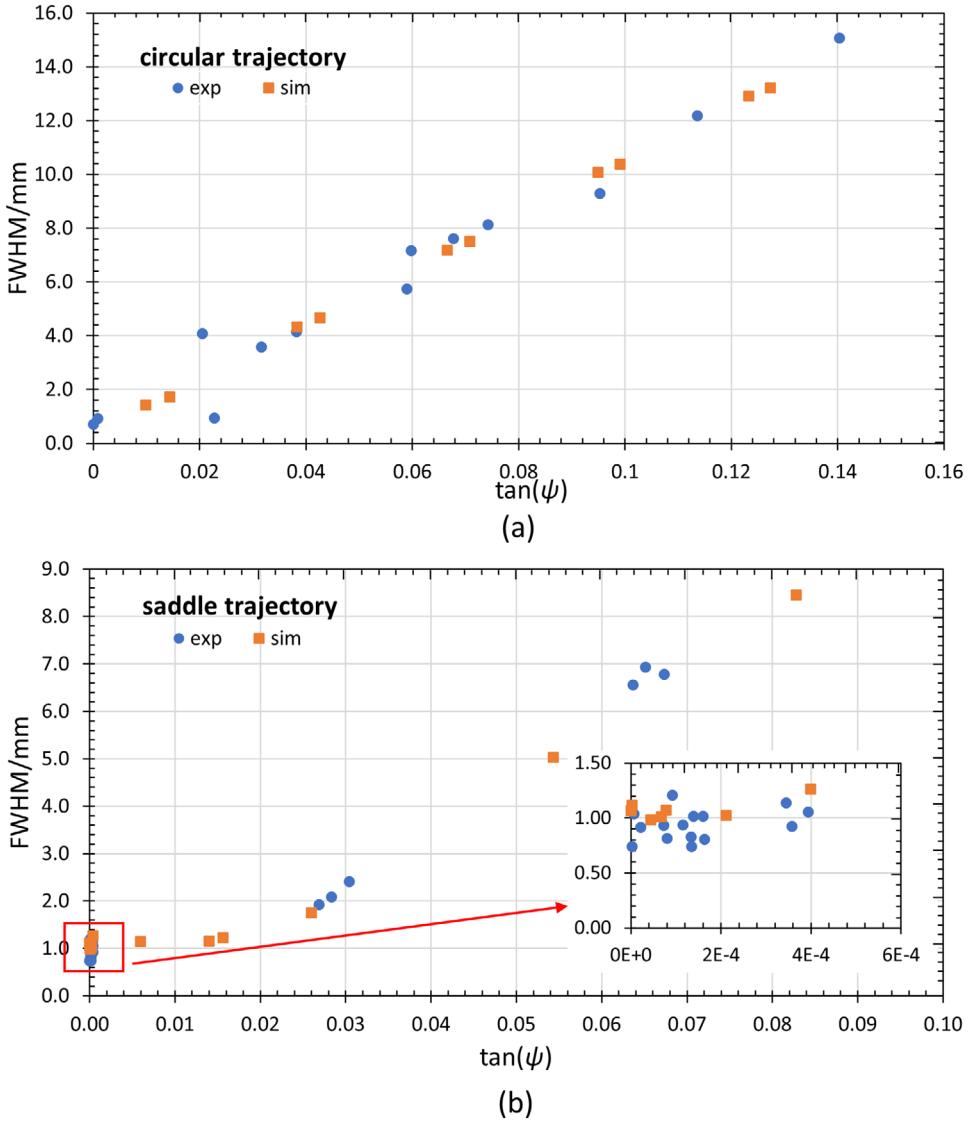

FIGURE 5 The scatter plot of FWHM and tan(ψ). (a) Measured FWHM and tan(ψ) from simulations and three circular trajectory scans. (b) Measured FWHM and tan(ψ) from simulations and three saddle trajectory scans. The zoom-in shows the points located around the y-axis. Blue points are data from the real experiment. Orange points are data from simulations. FWHM, full width half maximum.

immobile in a fixed coordinate system, therefore the nine-degrees-of-freedom flexmap calibration compensates for all known gravity effects within the gantry.[29] For the yaw motion presented in this study, the floor flatness was the main reason for the artifacts. Since we cannot ensure that the yaw motion is executed by driving through the same path on the floor as shown in Figure 3, a scan-specific correction is needed. The reconstructed images after correction showed the disk thickness was around 1 mm, and the actual disk thickness was 1.00 mm according to our measurement using a caliper with a precision of 0.05 mm, showing that IR tracking achieved a satisfactory correction precision. Otherwise, the spatial resolution on the axial plane was greatly improved from 0.37 to 0.98 lp/mm when performing saddle trajectory with IR tracking, which was at the same level as the linac mounted CBCT scanner. IR tracking is thus feasible and provides accurate corrections for irregular trajectory scans with yaw motion executed by the robotic CBCT scanner used in this study.

We evaluated the saddle trajectory scan with the incompleteness map. This metric provided a continuous value to evaluate to which extent a point P dissatisfied Tuy's condition with the heuristic adaptation to account for the finite detector size suggested by Sun et al.[28] According to Figure 5, we can see that there was a strong relationship between the artifacts and the incompleteness value. However, this did not mean a large incompleteness value would surely introduce CB artifacts. The incompleteness value only represented the data insufficiency at point P, whether there will be obvious artifacts also depended on the shape,

24734209, 0, Downloaded from https://aapm.onlinelibrary.wiley.com/doi/10.1002/mp.16943 by Cochrane Germany, Wiley Online Library on [21/02/2024]. See the Terms and Conditions (https://onlinelibrary.wiley.com/terms-and-conditions) on Wiley Online Library for rules of use; OA articles are governed by the applicable Creative Commons License

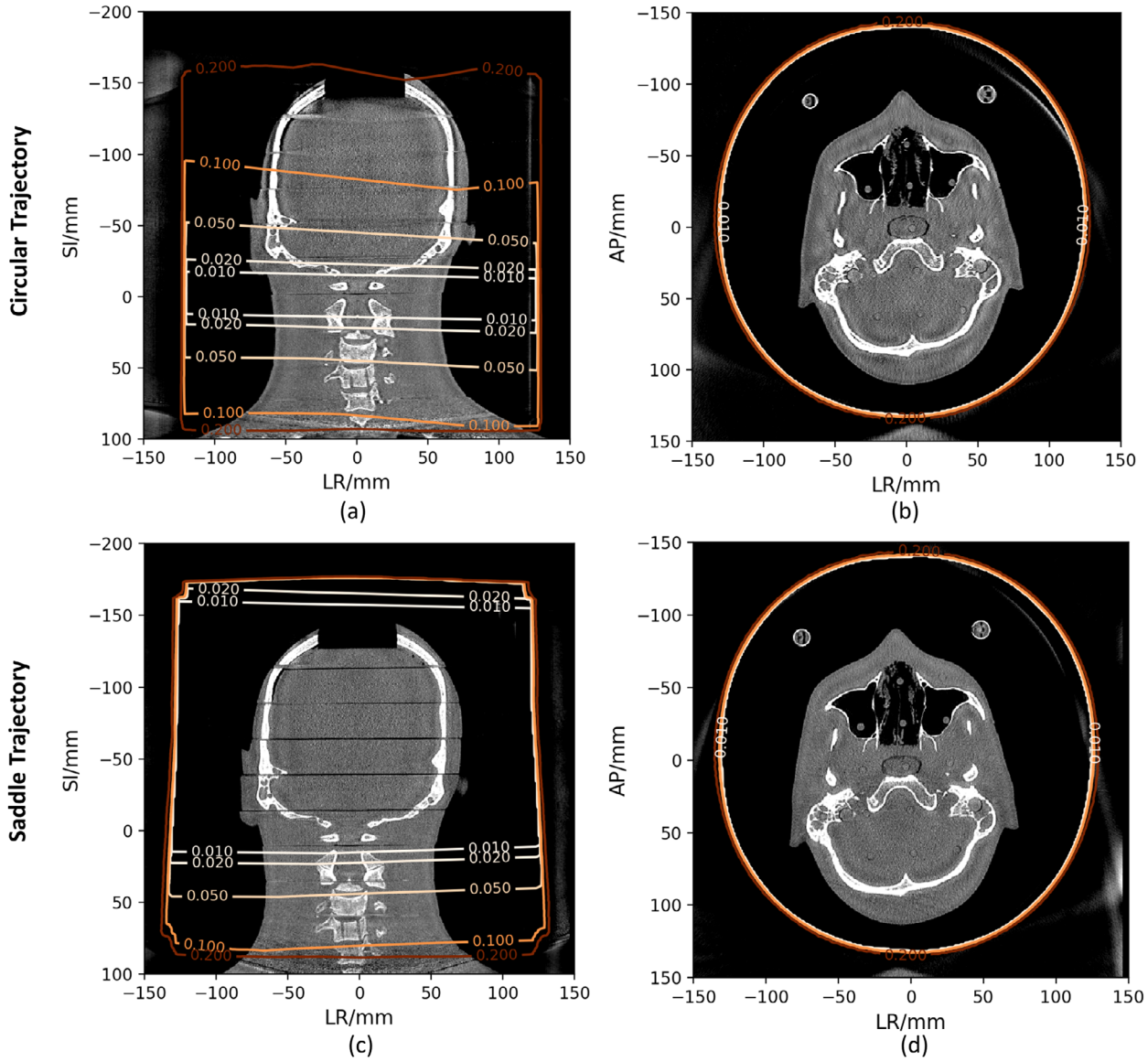

FIGURE 6 Alderson phantom with tan(ψ) isoline plot. (a) Coronal plane from the circular trajectory scan. (b) Axial plane taken at −21 mm in SI direction. (c) Coronal plane from the saddle trajectory scan. (d) Axial plane taken at −21 mm in SI direction. Solid lines indicate the value of tan(ψ). (window level: 0.0207, window width: 0.0286). SI, superior-inferior.

direction, and material of the object at that point. As shown in Figure 6a, although the incompleteness value was very large at the top of the head, there were no obvious artifacts for the bone. In general, a large incompleteness value represents a high possibility of showing CB artifacts, which undermines the reliability of a high incompleteness value region. Therefore the incompleteness value is a useful metric to evaluate the performance of an irregular trajectory in terms of data sufficiency.

We also reconstructed the images using FDK reconstruction. The needed time for the reconstruction was 32 s, which was greatly reduced compared to more than 10 min of the iterative reconstruction approach without losing many details as shown in Figure S3. The short reconstruction time enabled us to check the corrected image shortly after the scan.

The novel CBCT system can also achieve tilt-based saddle trajectories with tilt angles (around the LR axis in Figure 1c) from −30° to 30°. In addition, the wheels under the gantry allow the system to move in four directions and achieve many other non-circular trajectories such as helical and circle-and-line CBCT scans. Our methods offer a feasible workflow to evaluate the many other possible non-circular CBCT trajectories.

In our work, we tried to avoid truncations during the scan. According to Pack et al.,[26] saddle trajectory scan images can be reliably reconstructed even when there

24734209, 0, Downloaded from https://aapm.onlinelibrary.wiley.com/doi/10.1002/mp.16943 by Cochrane Germany, Wiley Online Library on [21/02/2024]. See the Terms and Conditions (https://onlinelibrary.wiley.com/terms-and-conditions) on Wiley Online Library for rules of use; OA articles are governed by the applicable Creative Commons License

is axial truncation. The combination of axial and lateral truncations is more complex, see, for example, Gindrier et al.[35] If the images can be reliably reconstructed, iterative reconstruction should be accurate as long as the reconstructed image encompasses the part of the object seen by at least one x-ray beam.

In this study, we used a limited axial FOV. The CBCT system can achieve an axial FOV of 254.6 mm when the detector is centered (by shifting the detector laterally up to 490 mm FOV is achievable). This may lead to lateral truncation when scanning the chest and pelvis sites. One can achieve a large field-of-view by joining two small field-of-view images, as demonstrated by Belotti et al.[36] and Karius et al.[37] for circular trajectories.

5 | CONCLUSION

In conclusion, we successfully acquired saddle trajectory CBCT scans with a novel CBCT system combined with IR tracking. A geometrical quantity incompleteness was used to evaluate the performance of this irregular trajectory and found a strong relationship with CB artifacts above the threshold of 0.02. Our results showed that saddle trajectories provide a much larger reliably reconstructed region than conventional circular CBCT scans. The same workflow can be used to explore other non-circular trajectories in the future.

ACKNOWLEDGMENTS

The purchase of the robotic CBCT scanner of the Department of Medical Physics of the Faculty of Physics of the LMU was funded by the Deutsche Forschungsgemeinschaft (DFG), grant number INST 86/2120-1 FUGG.

Open access funding enabled and organized by Projekt DEAL.

CONFLICT OF INTEREST STATEMENT

The Department of Radiation Oncology of the LMU University Hospital and the Department of Medical Physics of the Faculty of Physics of the LMU each have a research agreement with medPhoton GmbH.

REFERENCES

1. Baba R, Ueda K, Okabe M. Using a flat-panel detector in high resolution cone beam CT for dental imaging. *Dentomaxillofac Radiol*. 2004;33:285-290.
2. Kapila SD, Nervina JM. CBCT in orthodontics: assessment of treatment outcomes and indications for its use. *Dentomaxillofac Radiol*. 2015;44:20140282.
3. Jaffray DA, Drake DG, Moreau M, Martinez AA, Wong JW. A radiographic and tomographic imaging system integrated into a medical linear accelerator for localization of bone and soft-tissue targets. *Int J Radiat Oncol Biol Phys*. 1999;45:773-789.
4. Barney BM, Lee RJ, Handrahan D, Welsh KT, Cook JT, Sause WT. Image-Guided Radiotherapy (IGRT) for prostate cancer comparing kV imaging of fiducial markers with cone beam computed tomography (CBCT). *Int J Radiat Oncol Biol Phys*. 2011;80:301-305.
5. Dzierma Y, Beyhs M, Palm J, et al. Set-up errors and planning margins in planar and CBCT image-guided radiotherapy using three different imaging systems: a clinical study for prostate and head-and-neck cancer. *Physica Med*. 2015;31:1055-1059.
6. Rafferty MA, Siewerdsen JH, Chan Y, et al. Investigation of C-Arm Cone-Beam CT-Guided Surgery of the Frontal Recess:. *Laryngoscope*. 2005;115:2138-2143.
7. Siewerdsen JH. Cone-beam CT with a flat-panel detector: from image science to image-guided surgery. *Nucl Instrum Methods Phys Res, Sect A*. 2011;648:S241-S250.
8. Karius A, Strnad V, Lotter M, Kreppner S, Bert C. First clinical experience with a novel, mobile cone-beam CT system for treatment quality assurance in brachytherapy. *Strahlenther Onkol*. 2022;198:573-581.
9. Tuy HK. An inversion formula for cone-beam reconstruction. *SIAM J Appl Math*. 1983;43:546-552.
10. Finch DV. Cone beam reconstruction with sources on a curve. *SIAM J Appl Math*. 1985;45:665-673.
11. van Straten M, Venema H, Majoie C, Freling N, Grimbergen C, den Heeten G. Image quality of multisection CT of the brain: thickly collimated sequential scanning versus thinly collimated spiral scanning with image combining. *Am J Neuroradiol*. 2007;28:421-427.
12. Nikupaavo U, Kaasalainen T, Reijonen V, Ahonen S-M, Kortesniemi M. Lens dose in routine head CT: comparison of different optimization methods with anthropomorphic phantoms. *Am J Roentgenol*. 2015;204:117-123.
13. Yamagami T, Kato T, Iida S, Hirota T, Nishimura T. Percutaneous needle biopsy for small lung nodules beneath the rib under CT scan fluoroscopic guidance with Gantry Tilt. *Chest*. 2004;126:744-747.
14. Tersol A, Wu P, Clackdoyle R, Boone JM, Siewerdsen JH. Sampling effects for emerging cone-beam CT systems and scan trajectories: from Tuy's condition to system design and routine image quality tests. In: Zhao W, Yu L, eds. *Medical Imaging 2022: Physics of Medical Imaging*. SPIE; 2022:55.
15. Gang GJ, Siewerdsen JH, Stayman JW. Non-circular CT orbit design for elimination of metal artifacts. In: Bosmans H, Chen G-H, eds. *Medical Imaging 2020: Physics of Medical Imaging*. SPIE; 2020:79.
16. Stayman JW, Capostagno S, Gang GJ, Siewerdsen JH. Task-driven source–detector trajectories in cone-beam computed tomography: I. Theory and methods. *J Med Imaging*. 2019;6:1.
17. Wu P, Sheth N, Sisniega A, et al. C-arm orbits for metal artifact avoidance (MAA) in cone-beam CT. *Phys Med Biol*. 2020;65:165012.
18. Hosoo H, Ito Y, Marushima A, et al. Image quality improvements for brain soft tissue in neuro-endovascular treatments: a novel dual-axis "butterfly" trajectory for optimized cone-beam CT. *Eur J Radiol*. 2023;160:110713.
19. Ma YQ, Gang GJ, Ehtiati T, et al. Non-circular CBCT Orbit design and realization on a clinical robotic C-arm for metal artifact reduction. In: Linte CA, Siewerdsen JH, eds. *Medical Imaging 2022: Image-Guided Procedures, Robotic Interventions, Modeling*. SPIE; 2022:8.
20. Reynolds T, Ma Y, Wang T, et al. Revealing pelvic structures in the presence of metal hip prothesis via non-circular CBCT orbits. *Proc SPIE-Int Soc Opt Eng*. 2023;12466:124660Y.
21. Katsevich A. Theoretically exact filtered backprojection-type inversion algorithm for spiral CT. *SIAM J Appl Math*. 2002;62:2012-2026.
22. Noo F, Pack J, Heuscher D. Exact helical reconstruction using native cone-beam geometries. *Phys Med Biol*. 2003;48:3787-3818.

24734209, 0, Downloaded from https://aapm.onlinelibrary.wiley.com/doi/10.1002/mp.16943 by Cochrane Germany, Wiley Online Library on [21/02/2024]. See the Terms and Conditions (https://onlinelibrary.wiley.com/terms-and-conditions) on Wiley Online Library for rules of use; OA articles are governed by the applicable Creative Commons License

23. Yu H, Wang G. Studies on artifacts of the Katsevich algorithm for spiral cone-beam CT. In: U. Bonse, eds. *Developments in X-Ray Tomography IV*. SPIE; 2004:540.
24. Katsevich A. Image reconstruction for the circle and line trajectory. *Phys Med Biol*. 2004;49:5059-5072.
25. Katsevich A. Image reconstruction for the circle-and-arc trajectory. *Phys Med Biol*. 2005;50:2249-2265.
26. Pack JD, Noo F, Kudo H. Investigation of saddle trajectories for cardiac CT imaging in cone-beam geometry. *Phys Med Biol*. 2004;49:2317-2336.
27. Clackdoyle R, Noo F. Quantification of Tomographic Incompleteness in Cone-Beam Reconstruction. *IEEE Trans Radiat Plasma Med Sci*. 2020;4:63-80.
28. Sun T, Clackdoyle R, Kim J-H, Fulton R, Nuyts J. Estimation of Local Data-Insufficiency in Motion-Corrected Helical CT. *IEEE Trans Radiat Plasma Med Sci*. 2017;1:346-357.
29. Keuschnigg P, Kellner D, Fritscher K, et al. Nine-degrees-of-freedom flexmap for a cone-beam computed tomography imaging device with independently movable source and detector. *Med Phys*. 2017;44:132-142.
30. Zechner A, Stock M, Kellner D, et al. Development and first use of a novel cylindrical ball bearing phantom for 9-DOF geometric calibrations of flat panel imaging devices used in image-guided ion beam therapy. *Phys Med Biol*. 2016;61:N592.
31. Messner IM, Keuschnigg P, Stöllinger B, et al. Investigating focal spot position drift in a mobile imaging system equipped with a monobloc-based x-ray generator. *Med Phys*. 2023;1-12.
32. Rit S, Oliva MV, Brousmiche S, Labarbe R, Sarrut D, Sharp GC. The Reconstruction Toolkit (RTK), an open-source cone-beam CT reconstruction toolkit based on the Insight Toolkit (ITK). *J Phys Conf Ser*. 2014;489:012079.
33. Götz S, Dickmann J, Rit S, et al. Evaluation of the impact of a scanner prototype on proton CT and helium CT image quality and dose efficiency with Monte Carlo simulation. *Phys Med Biol*. 2022;67:055003.
34. Chen B, Ramirez Giraldo JC, Solomon J, Samei E. Evaluating iterative reconstruction performance in computed tomography. *Med Phys*. 2014;41:121913.
35. Gindrier N. *Reconstruction cone-beam à partir de projections avec troncations transverses*. PhD thesis, 2022. Thèse de doctorat dirigée par Desbat, Laurent et Clackdoyle, Rolf Mathématiques appliquées Université Grenoble Alpes 2022.
36. Belotti G, Fattori G, Baroni G, Rit S. Extension of the cone-beam CT field-of-view using two complementary short scans. *Med Phys*. 2023;1-14.
37. Karius A, Szkitsak J, Strnad V, Fietkau R, Bert C. Cone-beam CT imaging with laterally enlarged field of view based on independently movable source and detector. *Med Phys*. 2023;50:5135-5149.

SUPPORTING INFORMATION

Additional supporting information can be found online in the Supporting Information section at the end of this article.

How to cite this article: Wei C, Albrecht J, Rit S, et al. Reduction of cone-beam CT artifacts in a robotic CBCT device using saddle trajectories with integrated infrared tracking. *Med Phys*. 2024;1-13. https://doi.org/10.1002/mp.16943

24734209, 0, Downloaded from https://aapm.onlinelibrary.wiley.com/doi/10.1002/mp.16943 by Cochrane Germany, Wiley Online Library on [21/02/2024]. See the Terms and Conditions (https://onlinelibrary.wiley.com/terms-and-conditions) on Wiley Online Library for rules of use; OA articles are governed by the applicable Creative Commons License